

# A dynamic atlas of interference patterns in superimposed, opposite sense ductile shear zones

M.A. Finch<sup>a,b</sup>, P.D. Bons<sup>c</sup>, R.F. Weinberg<sup>b</sup>,  
M.-G. Llorens<sup>d</sup>, A. Grier<sup>e</sup>, and E. Gomez-Rivas<sup>f</sup>

<sup>a</sup> Department of Earth and Environmental Sciences, James Cook University, Townsville, Queensland, Australia

<sup>b</sup> School of Earth, Atmosphere and Environment, Monash University, Clayton, Victoria, 3800, Australia

<sup>c</sup> Department of Geosciences, Eberhard Karls University Tübingen, Wilhelmstr. 56, 72074 Tübingen, Germany

<sup>d</sup> Geosciences Barcelona CSIC, Lluís Sole i Sabaris s/n, 08028, Barcelona, Spain

<sup>e</sup> Departament de Geologia, Universitat Autònoma de Barcelona, 08193 Bellaterra (Cerdanyola del Vallès), Spain

<sup>f</sup> Departament de Mineralogia, Petrologia i Geologia Aplicada, Universitat de Barcelona, 080280 Barcelona, Spain

**ABSTRACT:** Ductile shear zones that reactivate a coplanar shear zone with opposite shear sense are known from a variety of tectonic environments. Recognition of reactivation requires understanding the interference patterns that form when microstructures produced in the first event (D1) are modified by the second event (D2). We use numerical modelling to demonstrate the effect of D1 structures on the development of shear zone interference patterns during a coplanar, opposite sense D2 ductile shearing event. Seven models were generated from increasing D1 dextral simple shear strains ( $\gamma_{\text{dextral}} = 2-14$ ) and we then superimposed D2 sinistral shearing ( $\gamma_{\text{sinistral}} = 10$ ). The interference patterns produced are highly variable with geometric relationships between weak layers and strong lithons determining deformation style. Shear zones with high D1 strain can more easily accommodate D2 strain because more strain is localised into long, weak phase C planes, which are readily inverted and reused during sinistral shear. Interference structures in models and naturally deformed rocks include rotated  $\sigma$ -clasts, folded D1 S planes, disharmonic and hook folds, and cusped layers of weak phase. We present a dynamic atlas of interference patterns produced due to overprinting shear zones to facilitate identification of these zones in nature.

This manuscript is published in the *Journal of Structural Geology* (2022), 165, 104739. DOI: [10.1016/j.jsg.2022.104739](https://doi.org/10.1016/j.jsg.2022.104739). This is an author version of the article. For the final copy-edited version, please visit:

<https://www.sciencedirect.com/science/article/abs/pii/S0191814122002310>

**Keywords:** Shear zone; Numerical modelling; Microstructures; Opposite shear sense; Shear zone interference patterns; Inversion; Reactivation

## Highlights:

- Overprinting of D1 shear by opposite sense, coplanar D2 creates interference patterns.
- Interference patterns vary over short length and time scales.
- High strain during D1 makes transposition to D2 structures quicker
- Low strain during D1 results in a large decrease in strain localisation at the start of D2.
- Interference patterns in models are similar to those in naturally deformed rocks.

## 1. Introduction

Deciphering the tectonic history of deformed terranes commonly requires determination of shear sense in ductile shear zones. Research on shear sense indicators has identified a number of kinematic indicators at the macro- and micro-scale, including S–C–C' fabric, mica fish, veins,  $\sigma$ - and  $\delta$ -type porphyroclasts, porphyroblasts, cleavage, folds, and a number of flanking structures (e.g., Berthe et al., 1979; Grasemann and Stüwe, 2001; Griera et al., 2013; Holyoke and Tullis, 2006; Lister and Snoke, 1984; Llorens et al., 2013; Passchier and Simpson, 1986; White et al., 1986). One typical evolutionary pathway of anisotropic rocks under crystal plastic flow during simple shearing is that foliation planes nucleate at an angle of  $45^\circ$  to the shear zone boundary (S planes) and then progressively rotate into parallelism with the direction of shearing and shear zone boundary to become C planes (Lister and Snoke, 1984). C planes are typically comprised of the weakest phase within the rock and they localise strain (Finch et al., 2020; Holyoke and Tullis, 2006).

In the absence of strain hardening processes, when deformation ceases in a shear zone, weak layers remain and can be reactivated during later deformation. The reactivation event may be with the same stress field orientation as that of the original event after a period of quiescence or it may be in a different orientation. In the latter, the orientation of the strain axes may be different and unrelated to that of the original shearing or the strain axes for the two events may be coplanar, with a simple switch in movement sense (e.g., Dutta and Mukherjee, 2019; Finch et al., 2014; Roberts et al., 2022; Wennberg, 1996).

One tectonic setting where coplanar reactivation with opposite shear sense is relatively common is regions of cycling between extension and shortening, which can be recognised in shear zones as thrust shear sense overprinting normal shear sense (or vice versa). For example, extension in back-arc basins causes decompression melting at depth and crustal underplating by mafic magma and weakening of rocks, priming back arcs as sites of strain localisation during later shortening due to collision or accretion at the tectonic margin (Hyndman et al., 2005). Tectonic switching between periods of extension and shortening is also a common feature of long-lived active margins, where slab roll-back can cause extension while flat subduction can cause thickening and extension, with strain commonly localised in the weak back arc (Collins, 2002; Trevisan et al., 2021).

When shear zones are reactivated with opposite shear sense a unique set of structures form as the pre-existing microstructure rotates and deforms to accommodate the new shear direction. These hybrid structures can be thought of as shear zone interference patterns, in keeping with the terminology used in the seminal work of Ramsay (1962) that detailed the interference patterns produced when a secondary set of folds refold an earlier set. Shear zone interference patterns have been studied in naturally deformed rocks and a particularly comprehensive account was provided by Wennberg (1996) in the dextral-sense Bergen Arc shear zone, which overprinted a section of a pre-existing sinistral sense shear zone. Both the sinistral shear zone and the dextral shear zone were preserved, with a transition zone between them where interference structures can be observed. Within the transition zone sinistral S and C' planes showed rotation and inversion of shear direction to accommodate dextral shearing, S planes were asymmetrically folded, and lozenge-shaped quartz veins were rotated and their tips isoclinally folded.

Aside from Wennberg (1996) and a few other exceptions (e.g., Cooper et al., 2010), detailed accounts of the formation of hybrid shear structures are relatively rare, despite the ubiquity of overprinting shear zones worldwide (see Dutta and Mukherjee, 2019 and references therein). This may be due to lack of recognition and understanding, since some hybrid structures are similar to those that form during a single simple shearing event, just slightly rotated or modified (e.g., rotation of D1 structures and formation of folds) and others are unusual and difficult to interpret (e.g., highly variable fold geometries, lozenge-shaped grains with folded tips, and disharmonic folds). Switches in movement direction are important to detect because they can modify the driving conditions for fluid migration and mixing of different fluid compositions; processes that have previously been associated with the formation of some hydrothermal ore deposits (Murphy et al., 2011; Yan et al., 2021).

While studies of naturally deformed rocks are useful for understanding shear zone interference patterns, they record only one snapshot of the whole evolution, produced by one set of geological and rheological conditions. Since the structures in ductile shear zones change dramatically from low to high finite strain, and on the basis of rheology, kinematics of deformation, strain rate and other factors, the snapshots in time and finite strain provided in naturally deformed rocks cannot capture the full variability of dynamic interference patterns. In contrast, numerical modelling affords control of all parameters and visualisation of the complete geometrical and mechanical evolution, providing an otherwise unavailable insight into shear zone evolution.

Of primary interest is the effect of the pre-existing microstructure on the development of the overprinting microstructure (e.g., Griera et al., 2020). For example, overprinting of D1 shear zones dominated by S fabric is likely to produce different hybrid structures to overprinting of D1 shear zones dominated by S–C–C' fabric. The effect of structural inheritance is easily explored using numerical modelling, where a range of D1 structures can be produced, and then overprinted by an opposite sense D2. We aim to understand the effect of pre-existing microstructure on the development of hybrid structures under simple shearing and present a dynamic atlas that depicts the range of interference structures that form over increasing finite strain. We use our results to understand microstructures in two naturally-deformed shear zones, the Zaskar shear zone from the NW Himalaya (e.g., Finch et al., 2014) and the Bergen Arc shear zone in Norway (Wennberg, 1996), both of which overprint a previous coplanar, opposite sense shear zone.

## 2. Method

We investigated the microstructural development of overprinting shear zones using the numerical modelling platform ELLE, which is designed to simulate microstructural development during deformation and metamorphism (<http://www.elle.ws>; Bons et al., 2008; Jessell et al., 2001; Piazzolo et al., 2019). Mineral grains are simulated in ELLE as polygons (known as flynns) that are comprised of boundary nodes (bnodes) connected with straight lines at double or triple junctions (Fig. 1). A grid of unconnected nodes (unodes) stores additional material information about the developing microstructure, including the strain rate and stress state (Fig. 1d). Additionally, a second layer of passive markers are used to track material displacement. The ELLE platform is coupled to the full-field viscoplastic deformation code (VPFFT) of Lebensohn and Rollett (2020). Each unode is taken as a crystallite of a mineral grain with its own crystallographic properties

and symmetry, and with a certain lattice orientation that evolves with deformation. Deformation is accommodated by dislocation glide on crystallographic slip systems and the glide along a slip system is described as simple shear ( $\dot{\gamma}_s$ ) parallel to that slip system ( $s$ ):

$$\dot{\gamma}_s = A \left( \frac{\sigma_{//s}}{\tau_s} \right)^n \quad (1)$$

where  $A$  is the pre-exponential (scaling) factor (set to unity for all phases and all slip systems),  $\sigma_{//s}$  is the deviatoric shear stress parallel to the slip-system  $s$ , and  $n$  is the stress exponent. The critical resolved shear stress,  $\tau_{CRSS}$ , is a term that determines the effective strength or resistance to shear of the slip system  $s$ . The mechanical properties of a phase are determined by its crystallographic properties and the  $\sigma_{//s}$ -values for each of the available slip systems. The VPFFT-code calculates the stress and velocity fields by summing the shear components along all slip systems and all elements for the given boundary conditions and local stress and strain-rate compatibility requirements. The method solves the visco-plastic deformation by means of a spectral solver based on the Fast Fourier Transform (FFT). Details of the VPFFT method are in Lebensohn (2001), Lebensohn et al. (2008), Lebensohn et al. (2009), Lebensohn and Rollett (2020), Montagnat et al. (2014). Details of coupling VPFFT with ELLE are in Griera et al. (2013), Llorens et al. (2016a), Llorens et al. (2016b), Llorens et al. (2017), Steinbach et al. (2016) and Gomez-Rivas et al. (2017).

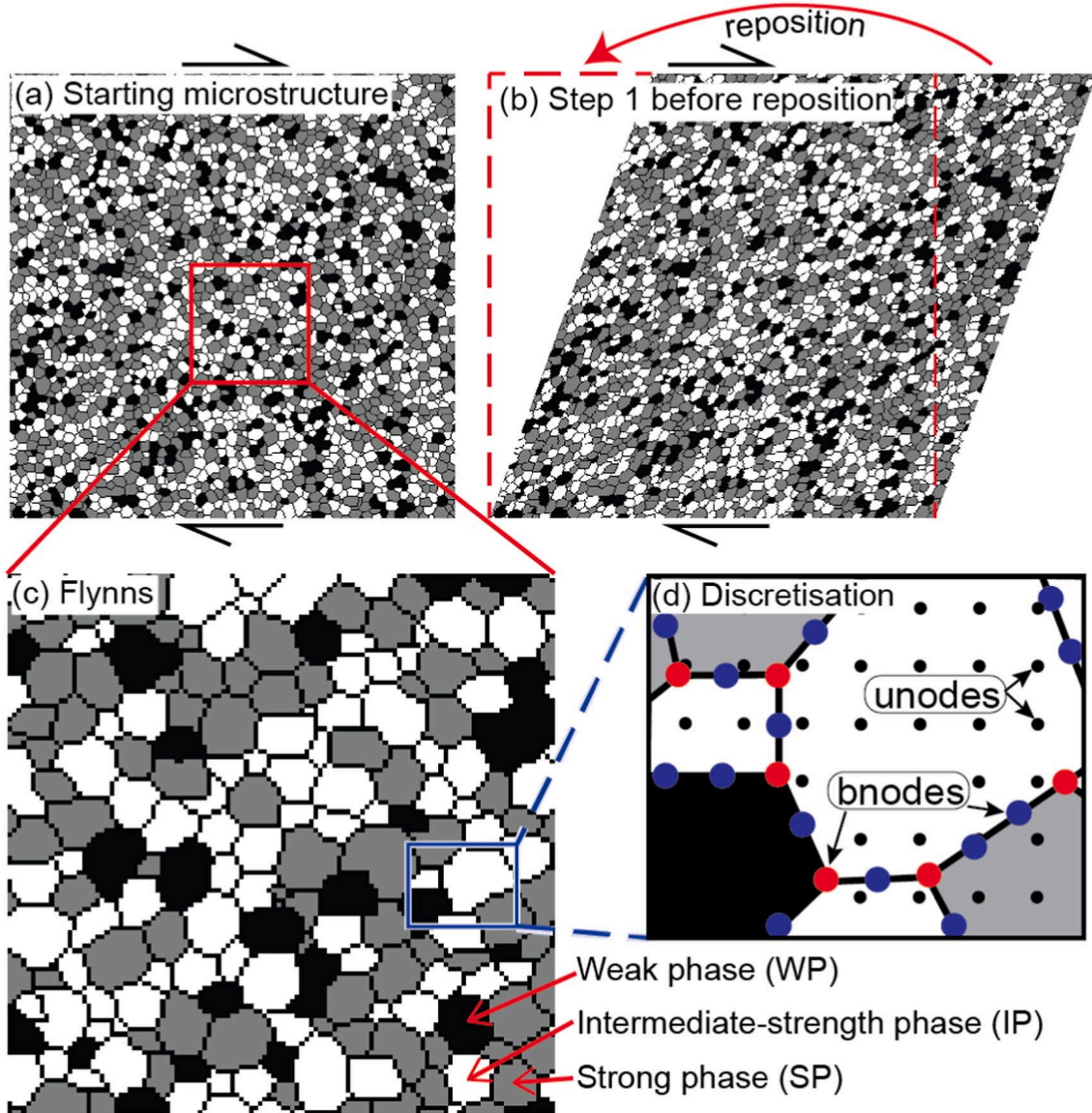


**Fig. 1.** A simplified depiction of the simulation process. (a) The starting microstructure consisting of three different phases. (b) After one step of dextral simple shear at  $\Delta\gamma = 0.02$ , grains that exit the model on the right re-enter on the left, forming a wrapping microstructure. (c) Zoomed view of the microstructure showing weak (black), intermediate-strength (white) and strong (grey) phases. (d) The discretisation of the grains (flynnns) as polygons formed by double (blue) and triple (red) boundary nodes (bnodes) connected by straight lines. Unconnected nodes (unodes) record information about the developing microstructure at each step of the simulation, including stress and strain rate.

The spectral VPFFT solver requires a regular grid of  $N \times N$  Fourier points (equivalent to unodes in ELLE), whereby  $N$  must be a power of two and here  $N = 256$  was used. The model boundaries are periodic and the unit cell is maintained by wrapping of material that leaves the model on one side to re-enter on the opposite side (see reposition step in Fig. 1b). The displacement of material points and bnodes that define phase boundaries is calculated by linear interpolation of the velocity field for the given time step. A deformation step causes the position of Fourier points to deviate from a regular grid and points are subsequently repositioned into a new square unit cell, making use of the periodic boundaries. Properties of the Fourier points in the new rectangular grid are interpolated from those of material points (Griera et al., 2011, 2013).

## 2.1. Model setup and visualisation

In order to understand the development of microstructures during co-planar shearing with opposite shear sense, we employed a three-phase microstructure with a weak phase (WP), intermediate-strength phase (IP) and strong phase (SP; Fig. 1). This microstructure was also employed by Finch et al. (2020) and aims to approximate a rock with biotite (WP), quartz (IP) and feldspar (SP), which is a relatively common composition for crustal shear zones in experimentally- and naturally-deformed rocks (e.g., Finch et al., 2014; Holyoke and Tullis, 2006). The models started with 2748 equant grains of which 15% were WP, 42.5% IP and 42.5% SP. The three phases were randomly distributed in a square model and velocity boundary conditions with constant strain rate were applied in simple shear increments of  $\Delta\gamma = 0.02$ . After each deformation step, the model was repositioned to the initial square unit cell and grain properties mapped back on to the grid before the next deformation step. A power-law viscous rheology (Eq. (1)) was employed with the stress exponent of the slip systems ( $n$ ) set to 3.

Each phase was associated with a different mineral model that specified the slip systems and their effective strength (resistance to shear,  $\tau_{CRSS}$ ). To model the WP we used a mineral model with hexagonal symmetry and three slip systems (basal, prismatic, and pyramidal), as in Griera et al. (2011, 2013), Ran et al. (2018), Llorens et al. (2019), and Finch et al. (2020). The intention of the WP is to approximate biotite and although mica is monoclinic, it has pseudo-hexagonal symmetry and its most important mechanical feature is a weak basal plane. Accordingly, we set the CRSS of the WP basal plane to one tenth of the WP non-basal planes, producing a mechanically anisotropic WP. We also employed a hexagonal mineral model for the SP, since feldspar is also pseudo-hexagonal, and set the effective strength of all its slip systems to 30x the strength of the WP basal plane. For the IP we used the crystal model of quartz with four slip systems (basal, prismatic, pyramidal  $\langle a \rangle$  and pyramidal  $\langle c+a \rangle$ ), all with an effective strength of 15x the strength of the WP basal plane (Griera et al., 2011, 2013). We assumed that the CRSS are constant and do not evolve during deformation.

Each hybrid model involved top-to-the-right (dextral) simple shear followed by top-to-the-left (sinistral) simple shear. To investigate the effect of the pre-existing structures on the development of hybrid structures we created seven models with different dextral finite shear strains of  $\gamma_{\text{dextral}} = 2, 4, 6, 8, 10, 12$  and 14. After the period of dextral shearing, the shear sense was reversed to sinistral shear until  $\gamma_{\text{sinistral}} = 10$ . We also included a sinistral shear only model ( $\gamma_{\text{dextral}} = 0$  to  $\gamma_{\text{sinistral}} = 10$ ) to compare to the hybrid models.

To understand microstructure development, we employ visualisations of the phase distribution as well as trace markers consisting of lines that were initially vertical at the start of dextral shearing and deformed under dextral then sinistral shear. We also employed visualisations of the stress and strain rate fields. The VPFIT code provides the deviatoric stress ( $S_{ij}$ ) and strain-rate ( $\dot{\epsilon}_{ij}$ ) tensors for each unode in the model and for each time step and from this we calculated the von Mises stress and strain rate, normalised to the mean value for the model. The von Mises stress ( $S_{VM}$ ) or strain rate ( $\dot{\epsilon}_{VM}$ ) is given by:

$$S_{VM} = \sqrt{\frac{2}{3} \mathbf{S}_{ij} \cdot \mathbf{S}_{ij}} \quad \text{and} \quad \dot{\epsilon}_{VM} = \sqrt{\frac{2}{3} \dot{\epsilon}_{ij} \cdot \dot{\epsilon}_{ij}} \quad (2)$$

In addition to qualitative description of the developing microstructure, we also calculated the Feret angle of the models using ImageJ (Schneider et al., 2012). The Feret angle is the orientation of the long axis of grains, where  $0^\circ$  (and  $180^\circ$ ) is parallel to the shear zone boundary (i.e., horizontal). We measured the Feret angle using increasing angles anticlockwise to  $x$ -positive axis, so that  $45^\circ$  is a dip of  $45^\circ$  left ( $S_{\text{dextral}}$  planes),  $135^\circ$  is a dip of  $45^\circ$  right ( $S_{\text{sinistral}}$  planes) and  $90^\circ$  is vertical. Data are presented as histograms of the proportion of each phase at each Feret angle. Since there are many small grains, calculating the proportion of grains at each Feret angle is not representative of the microstructure. Accordingly, the results are calculated as the proportion of the model area that is occupied by grains of WP/IP/SP at each Feret angle.

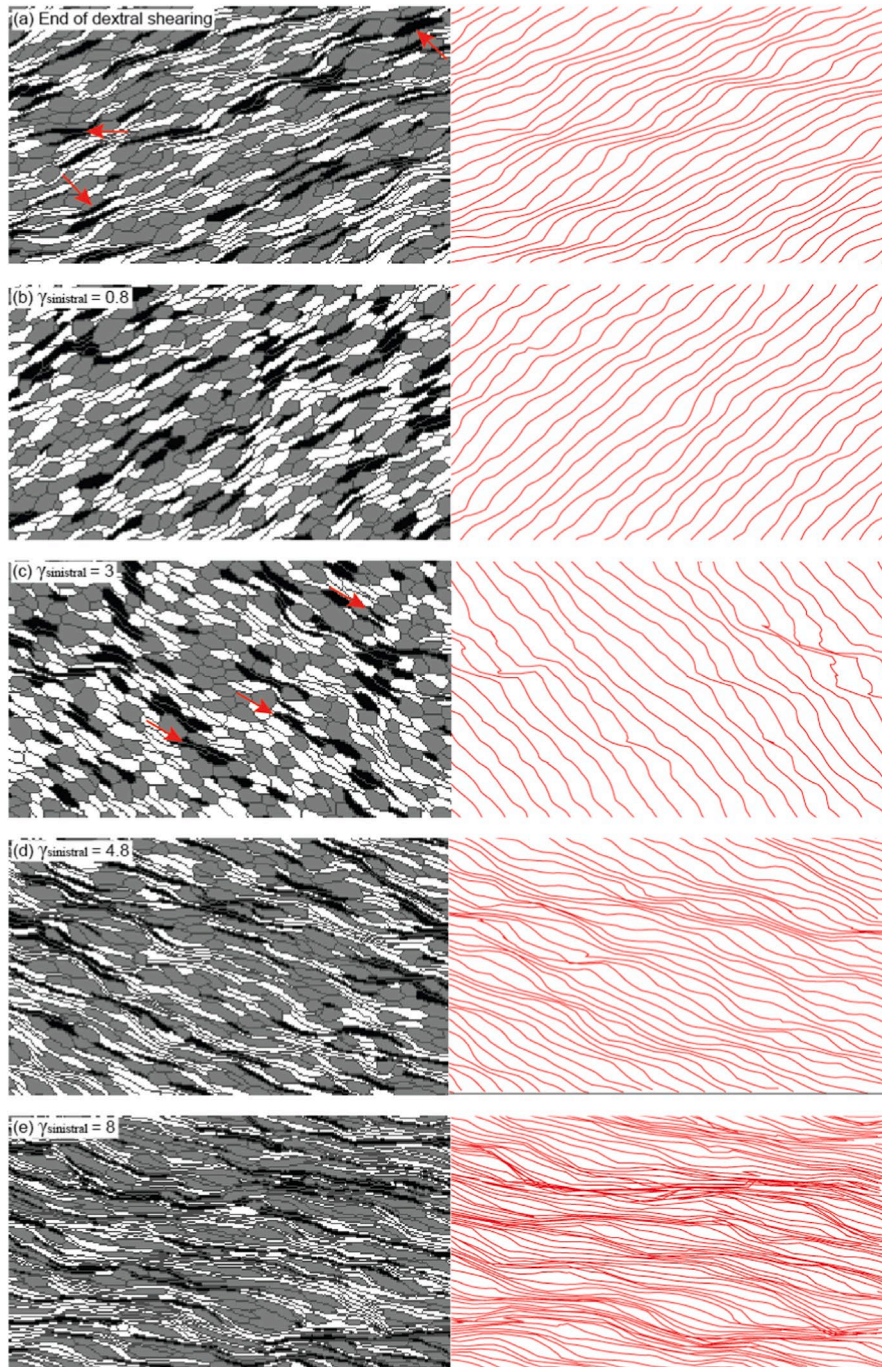
We also analysed the degree of strain localisation,  $F$ , calculated as

$$F = 1 - \frac{1}{N_u} \frac{(\sum \dot{\epsilon}_{vM})^2}{\sum \dot{\epsilon}_{vM}^2} \quad (3)$$

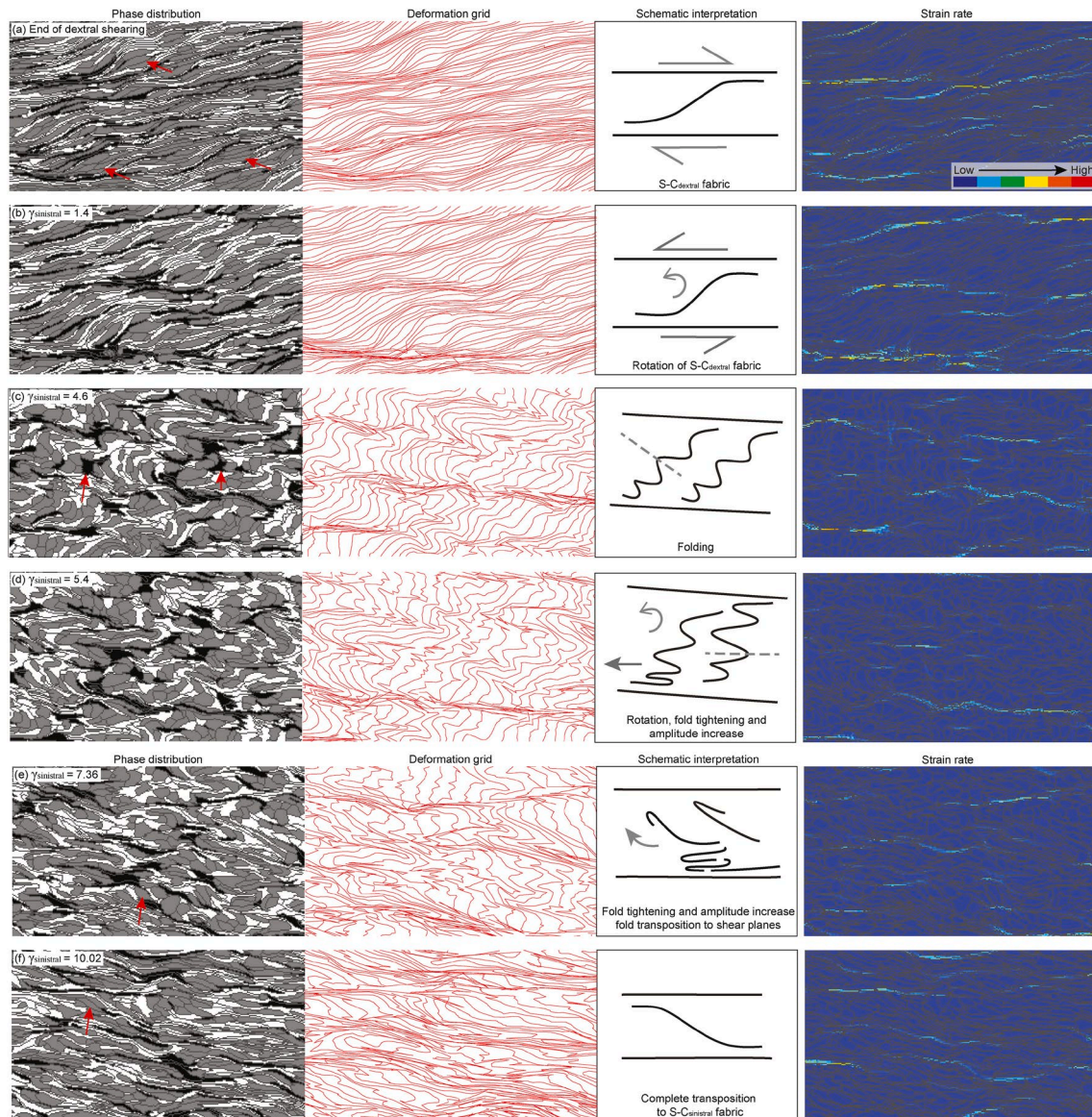
where  $N_u$  is the total number of unodes and  $\dot{\epsilon}_{vM}$  is the von Mises equivalent strain rate of each unode, as implemented by Steinbach et al. (2016).  $F$  ranges from 0 to 1, with 0 indicative of homogenous deformation and 1 indicating maximum localisation (where all strain is accommodated by a single unode, that is, a single point in the model).

### 3. Numerical results and interpretation

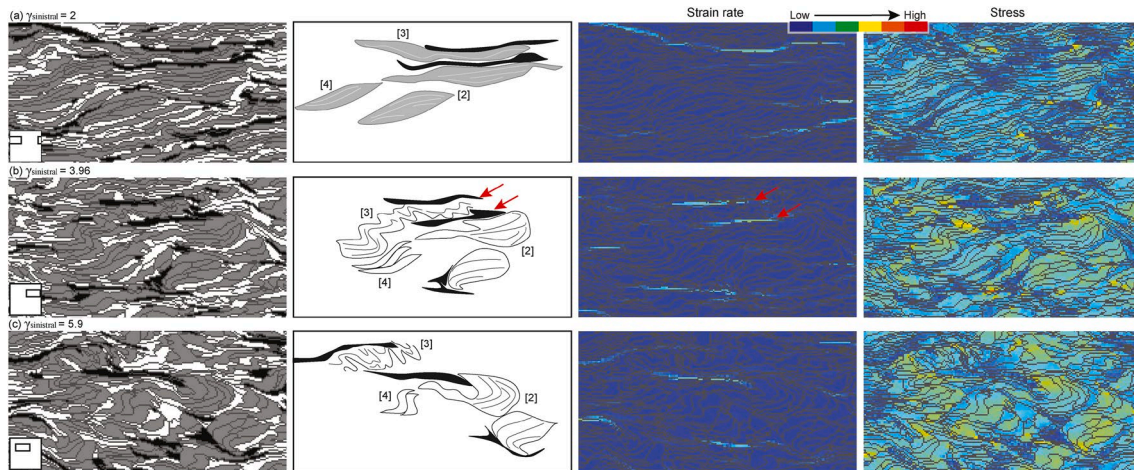
The microstructure produced during D1 dextral shearing affected the nature of the interference pattern that developed under D2 sinistral shearing, forming hybrid structures (Fig. 2, Fig. 3, Fig. 4, Fig. 5, Fig. 6, Fig. 7, Fig. 8). To ensure clarity when referring to structures that formed during dextral and sinistral shearing respectively, we use the subscript sinistral or dextral, so for example,  $S_{\text{sinistral}}$  planes are S planes that formed during sinistral shearing and  $C'_{\text{dextral}}$  shear bands are C' shear bands under dextral shearing. C planes are (sub-)parallel to the shear zone boundary, which is in the same orientation during dextral and sinistral shearing, so no distinction is made in that case. To understand when hybrid models have fully transposed to a sinistral shear microstructure, we compare the evolution of strain localisation and Feret angle to a model that has undergone sinistral shear only (Fig. 5, Fig. 6), so we describe the structures in that model briefly before exploring the hybrid models.



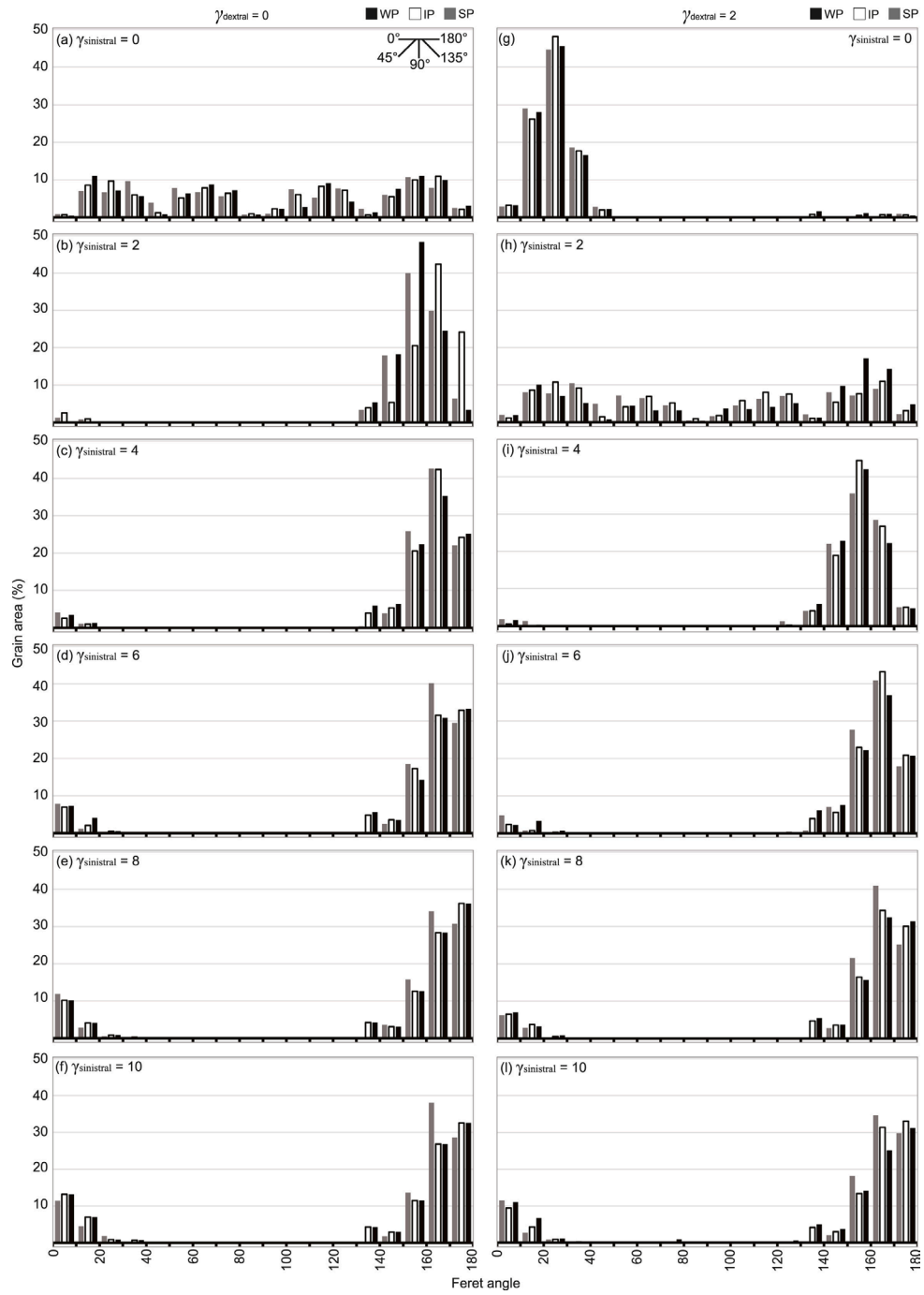
**Fig. 2.** Microstructural development (left) and passive deformation grids (right) of D1  $\gamma_{\text{dextral}} = 2$  followed by D2 sinistral shearing. (a) The microstructure at  $\gamma_{\text{dextral}} = 2$  is defined by S-fabric with minor isolated C planes. (b) After  $\gamma_{\text{sinistral}} = 0.8$  the microstructure has rotated anticlockwise and grains have shortened. (c) After  $\gamma_{\text{sinistral}} = 3$   $S_{\text{sinistral}}$  fabric dominates, with minor, isolated C planes. Note the absence of dextral or hybrid shear structures. (d) After  $\gamma_{\text{sinistral}} = 4.8$  grains of WP and IP are elongate and form S-C fabric while SP forms lozenge-shaped grains. (e) After  $\gamma_{\text{sinistral}} = 8$  sinistral S-C fabric dominates.

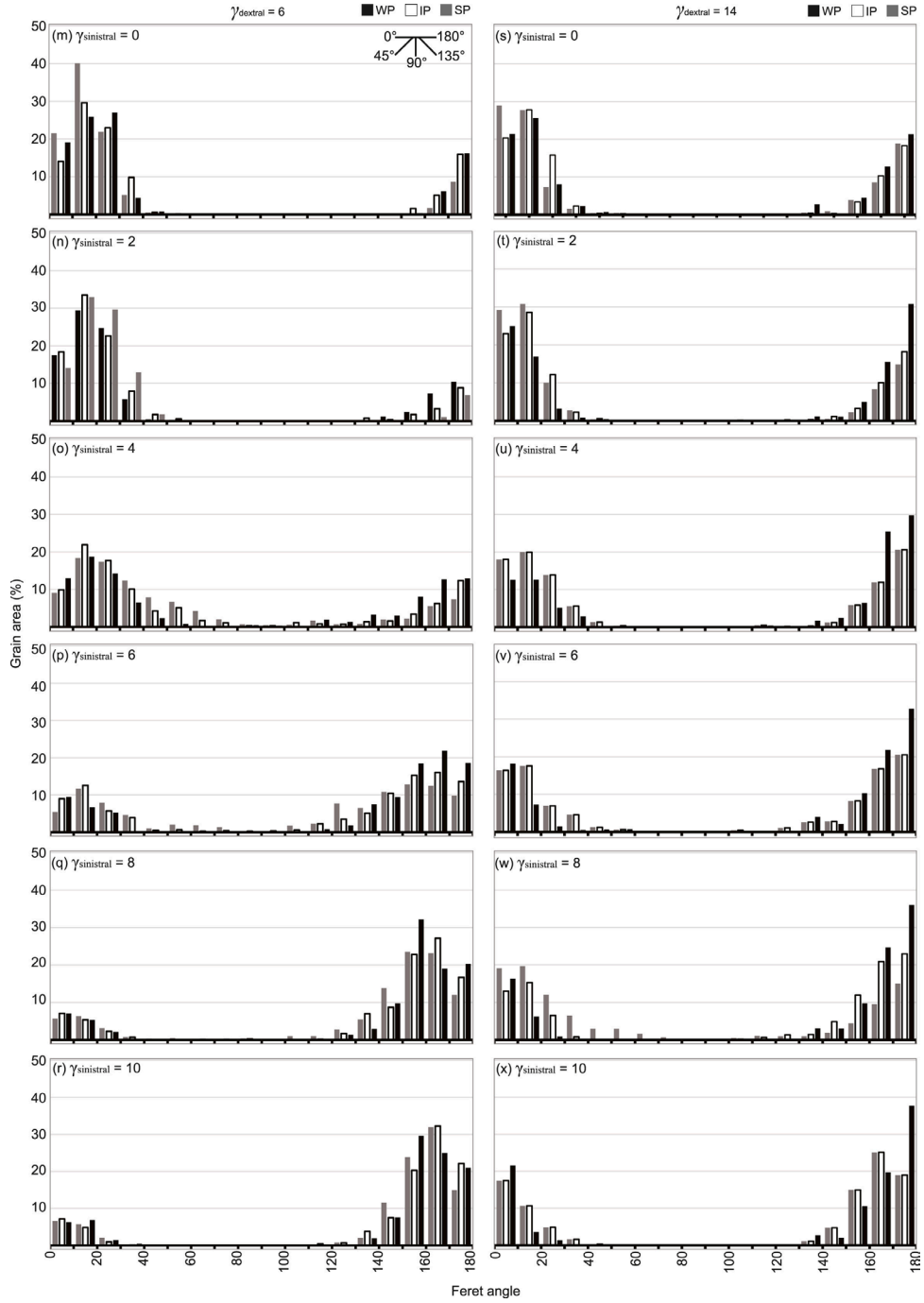


**Fig. 3.** Phase distribution, deformation grids, schematic interpretation of main structure and strain rate of  $\gamma_{\text{dextral}} = 6$  model under sinistral shearing. (a) The microstructure at  $\gamma_{\text{dextral}} = 6$  is defined by S-C fabric with a number of long shear planes with high strain rate that are defined by connected grains of WP. (b) After  $\gamma_{\text{sinistral}} = 1.4$  S planes have rotated anticlockwise to steeper angles, into parallelism with the maximum shortening direction. (c) Folds develop with axial planes perpendicular to the maximum shortening direction by  $\gamma_{\text{sinistral}} = 4.6$ . Note the irregular shape of WP grains and layers, forming tabular or triangular grains with pinched corners (arrows). (d) Folds rotate and stretch by  $\gamma_{\text{sinistral}} = 5.4$  so that the axial planes of most folds are parallel to the shear zone boundary. (e) Folds are isoclinal by  $\gamma_{\text{sinistral}} = 7.36$ , with axial planes parallel to C plane or S planes and attenuated or sheared off limbs. (f) By  $\gamma_{\text{sinistral}} = 10.02$  no evidence of hybrid structures remains.

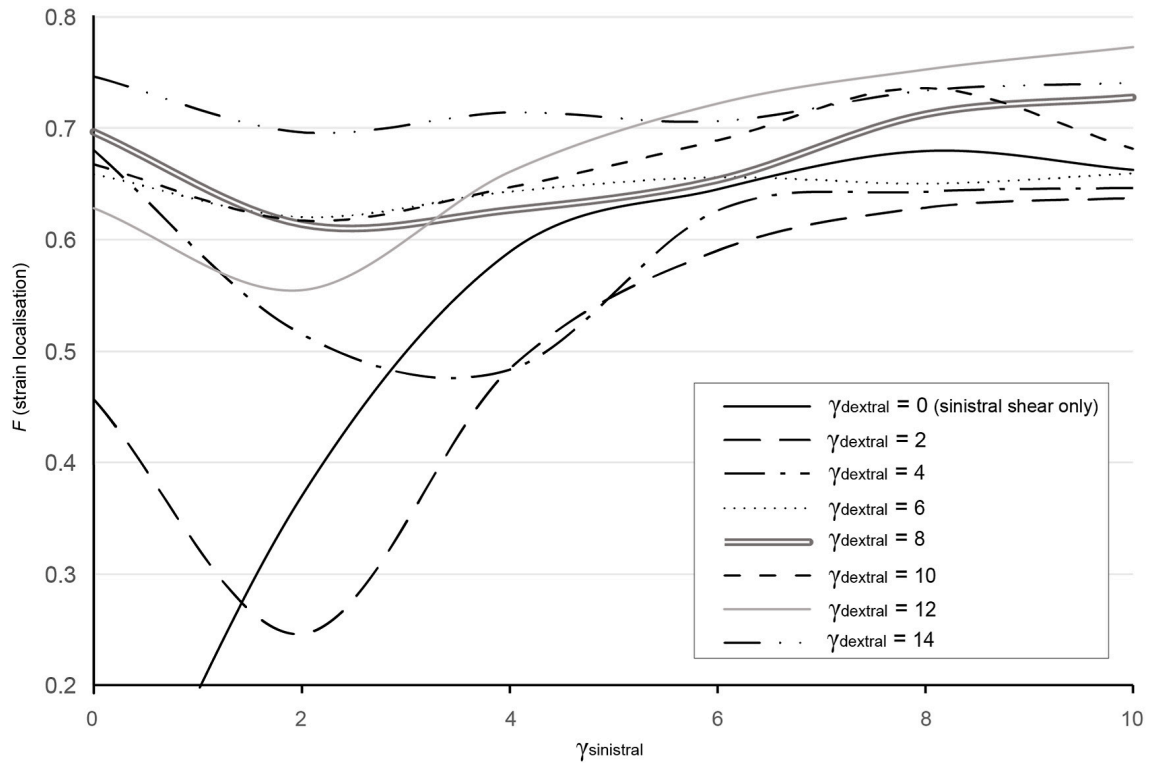


**Fig. 4.** The evolution of three D1/D2 interference structures that form in layers of strong phase with an interpretative sketch that highlights the features that demonstrate how the interference structures form and the strain rate and stress. The numbers in the sketch correspond to the number of the process that the layer undergoes, which are described in section 3.3.2. (a) Prior to the development of interference structures, layers of strong phase are parallel to  $S_{\text{dextral}}$  and C planes and form poorly defined  $\sigma_{\text{dextral}}$ -type objects (b) An intermediate stage in the formation of clear D1/D2 interference structures. The two SP layers labelled [2] are undergoing drag folding on the side of the layer that is adjacent to a high strain rate layer of WP. The SP layer labelled [3] is folding between two layers of WP that have different strain rates. The SP grains labelled [4] have rotated to steeper angles than in (a). (c) D1/D2 interference structures: [2] asymmetric isoclinal hook folds adjacent to layers of WP, [3] Disharmonic asymmetric folds between two layers of weak phase, [4] rotated  $\sigma_{\text{dextral}}$ -type objects. Images are from the  $\gamma_{\text{dextral}} = 14$  model. Inset in first column shows the position of the figure within the larger model, to allow comparison to movies of models (supplementary material).

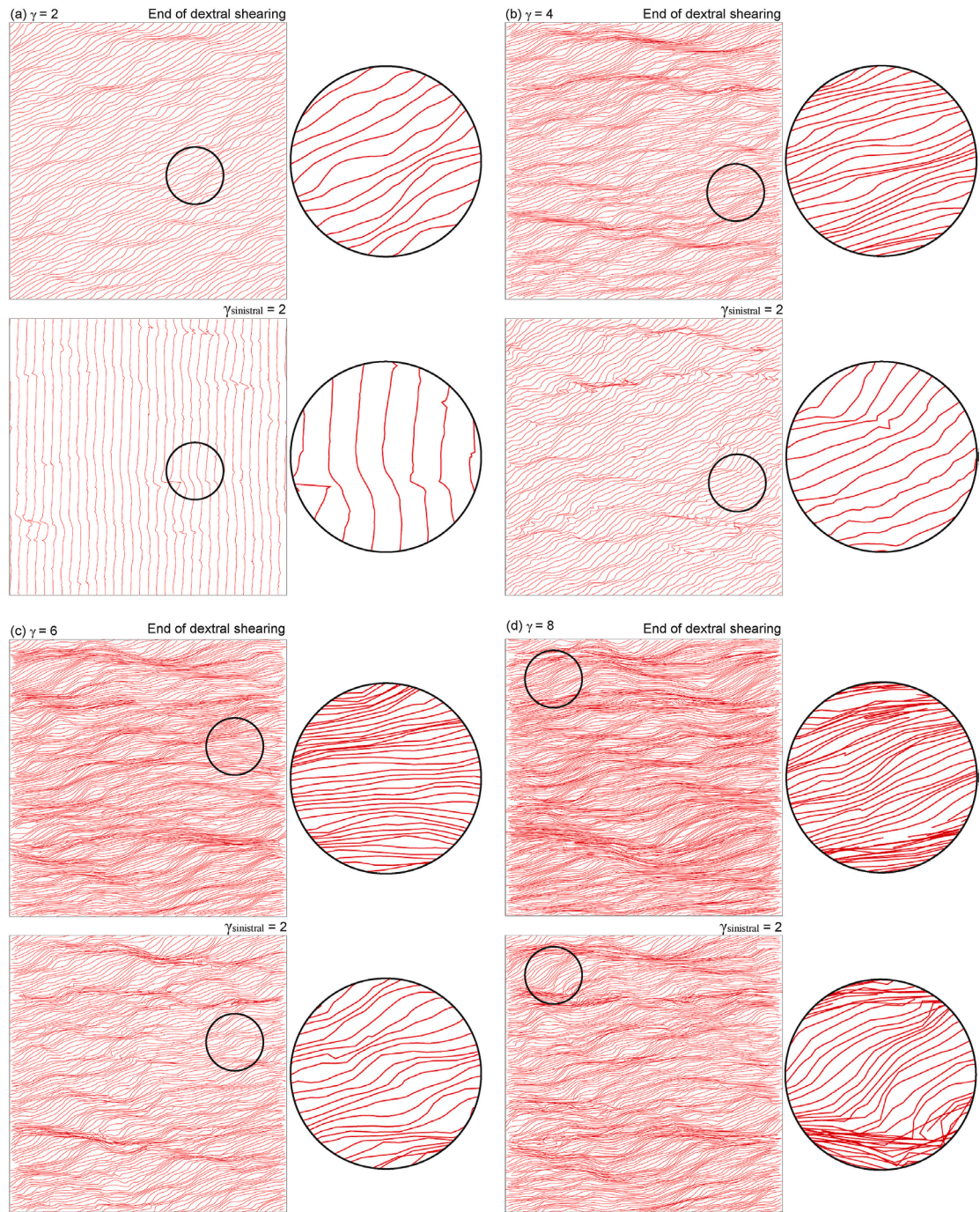




**Fig. 5.** Histograms of the distribution of Feret angles in grains of weak phase (WP), intermediate-strength phase (IP) and strong phase (SP). The first row of graphs is the Feret angle distribution at the end of dextral shearing, prior to sinistral shearing ( $\gamma_{\text{sinistral}} = 0$ ) and the graphs underneath are the Feret angle distribution at increasing finite strain in  $\Delta\gamma = 2$ . (a-f) Sinistral shear only (i.e., no prior dextral shearing), (g-l) Feret angle distribution in  $\gamma_{\text{dextral}} = 2$  model. The starting point shown in (g) shows all data concentrated on the left recording the result of early dextral shear. Note that by  $\gamma_{\text{sinistral}} = 4$  in (i) the distribution is similar to the sinistral shearing only model after the same amount of strain, shown in (c). (m-r) Feret angle distribution in  $\gamma_{\text{dextral}} = 6$  model. (s-x) Feret angle distribution in  $\gamma_{\text{dextral}} = 14$  model. Results are expressed as a proportion of grain area so that small grains do not skew results. Inset in (a) and (m) shows how the dip direction is indicated by the Feret angle.



**Fig. 6.** Strain localisation factor (F) over increasing finite strain in the seven hybrid models that involve D1 dextral shearing followed by D2 sinistral shearing and the sinistral shear only model for comparison. Note that all models with dextral shearing undergo strain delocalisation by  $\gamma_{\text{sinistral}} = 2-4$ .



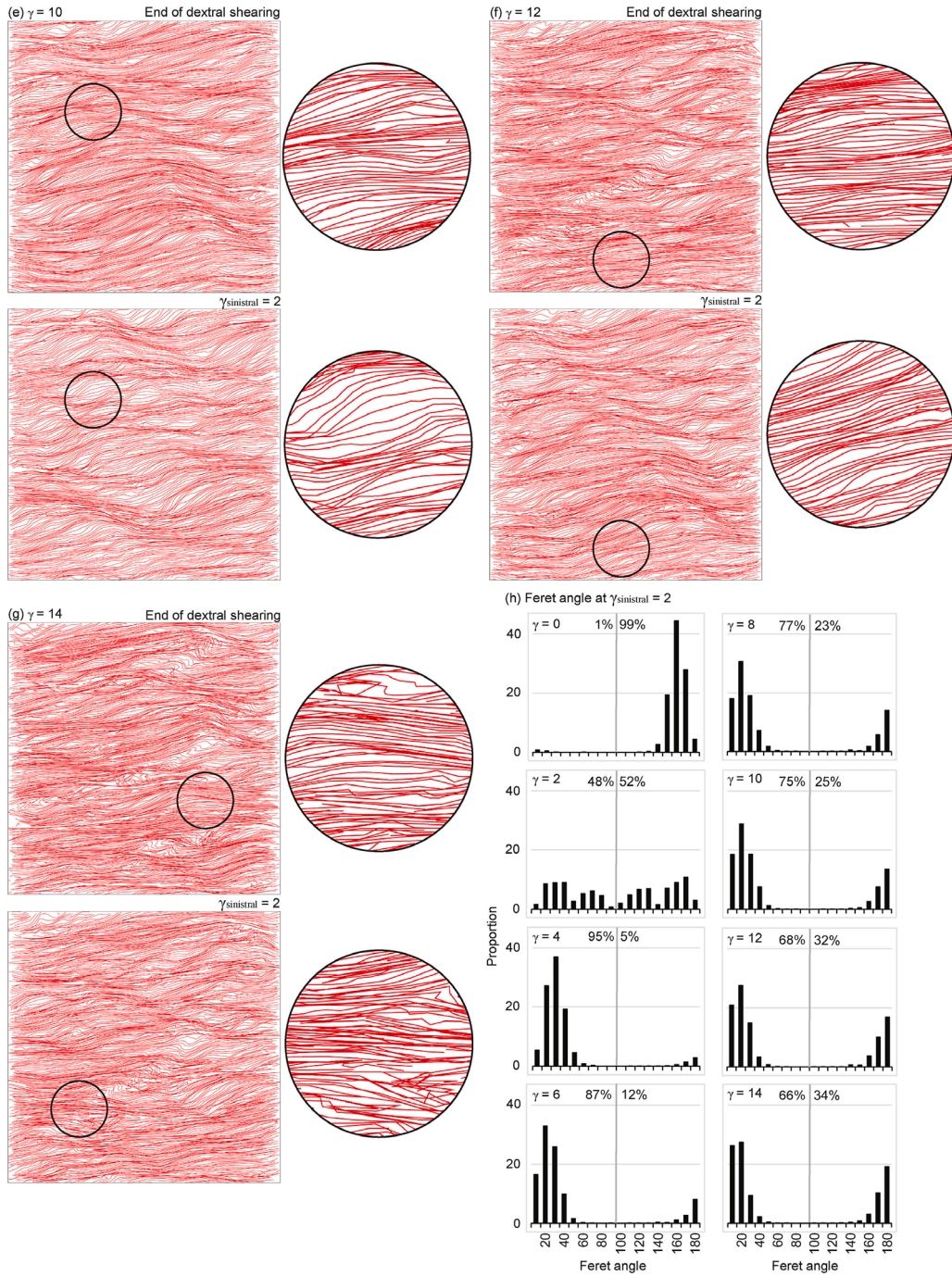


**Fig. 7.** Deformation grids for each hybrid model at the end of D1 dextral shearing and after  $\gamma_{\text{sinistral}} = 2$ . (a)  $\gamma_{\text{dextral}} = 2$  model, (b)  $\gamma_{\text{dextral}} = 4$  model, (c)  $\gamma_{\text{dextral}} = 6$  model, (d)  $\gamma_{\text{dextral}} = 8$  model, (e)  $\gamma_{\text{dextral}} = 10$  model, (f)  $\gamma_{\text{dextral}} = 12$  model, (g)  $\gamma_{\text{dextral}} = 14$  model, (h) Feret angle after  $\gamma_{\text{sinistral}} = 2$  in each model. The vertical line in each figure marks  $90^\circ$  (vertical) and the proportion of grains with angles  $< 90^\circ$  (dipping left, a result of dextral shearing) is indicated on the left of the line and the proportion of grains  $> 90^\circ$  (dipping right, a result of sinistral rotation) is on the right of the line.  $S_{\text{dextral}}$  planes have Feret angles  $\sim 10^\circ\text{-}45^\circ$  (dipping left) and  $S_{\text{sinistral}}$  planes  $\sim 135^\circ\text{-}170^\circ$  (dipping right). The figure demonstrates that models with higher dextral finite strain show quicker transposition to a sinistral microstructure, with a higher proportion of  $S_{\text{sinistral}}$  (right dipping) planes.

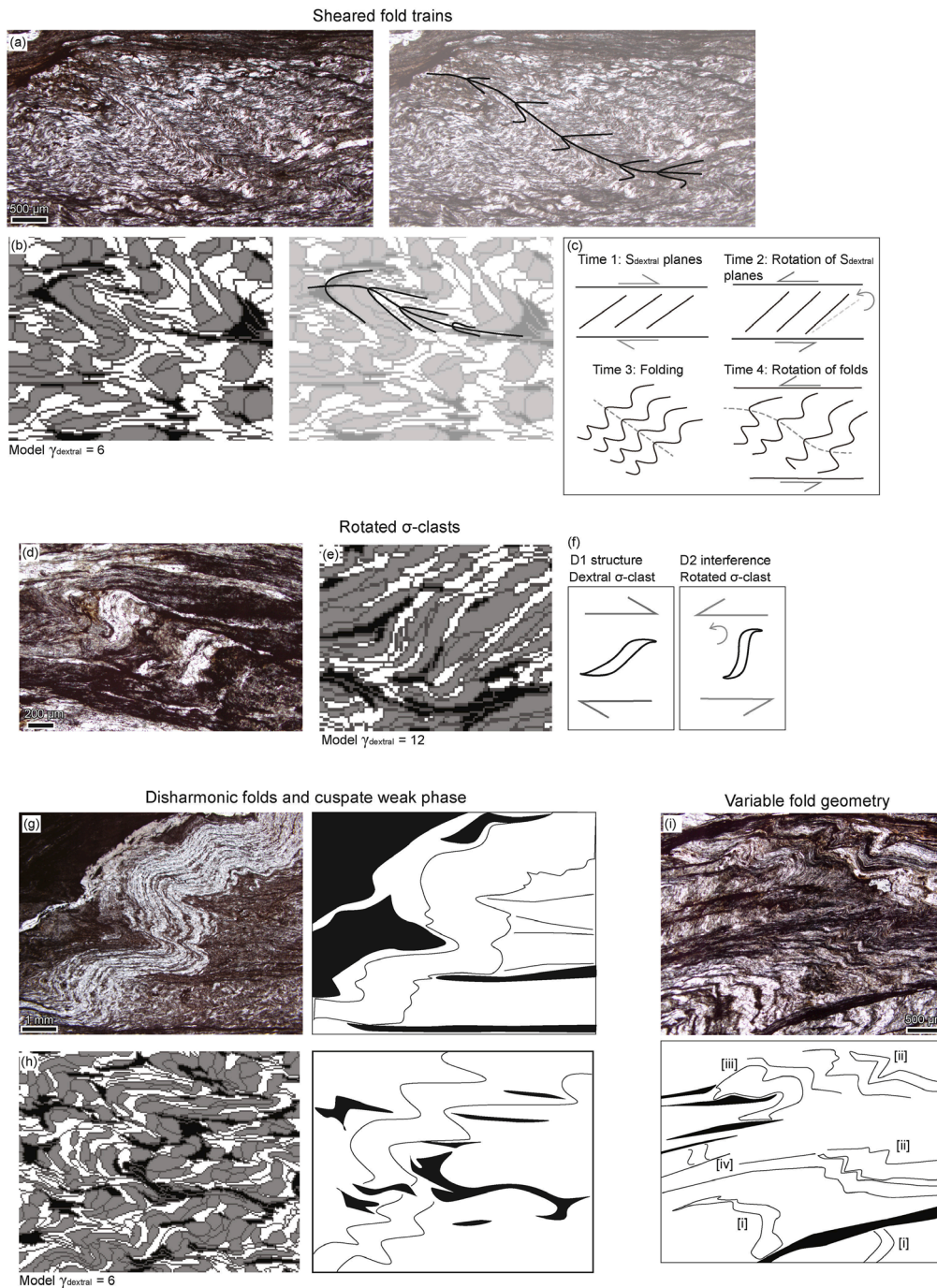


**Fig. 8.** Structures that form due to interference of D1 and D2 shear in the Zanskar shear zone (photomicrographs) and in the models, with interpretative sketches. (a-c) Sheared fold trains, (d-f) Rotated  $\sigma$ -clasts, (g-h) Disharmonic folds and cusped weak phase, (i) variable fold geometry. (a) Sheared fold trains composed of closed to isoclinal folds in thin section, (b) sheared fold trains in the model, (c) the evolution of sheared fold trains through the rotation of  $S_{\text{dextral}}$  planes into the maximum shortening direction, which causes folding. Shearing in adjacent layers of weak phase causes rotation of the folds. (d) Rotated  $\sigma$ -clast in quartz in thin section. (e) Rotated  $\sigma$ -clast in SP in model (f) structural evolution of rotated  $\sigma$ -clasts. (g) Disharmonic folds with cusped, discontinuous layers of weak phase in fold hinges in thin section. (h) Disharmonic folds in strong and intermediate-strength phase with cusped, discontinuous layers of weak phase in the model. (i) Photomicrograph showing (i) open folds, (ii) chevron folds, (iii) isoclinal folds, (iv) rotated planes with folded tips. A similar variety of fold types is seen in the models (e.g., Fig. 3, Fig. 4). All photomicrographs are under plane polarised light on a  $X$ - $Z$  section.

### 3.1. Sinistral shear-only model

In the sinistral shear-only model the grains start as equant (Fig. 1a), therefore with a random Feret angle (Fig. 5a) and by  $\gamma = 2$  all phases are elongate and dip right, with Feret angle maxima  $10^\circ$ – $30^\circ$  from the shear zone boundary (i.e., S planes; Fig. 5b). With increasing finite strain grains rotate towards parallelism with the shear zone boundary, with IP and WP rotating faster than the SP (Fig. 5c–f). By  $\gamma = 10$  S–C–C' fabric has developed, with most WP and IP grains close to parallel to the shear zone boundary, forming C planes, and SP  $10$ – $20^\circ$  from the shear zone boundary, forming S planes (Fig. 5f).

Consistent with the results of Finch et al. (2020), we find that the highest strain rate localises to layers of weak phase that are parallel to the shear zone boundary (supplementary movie: “Model\_sinistral\_strain” and “Model\_sinistral\_phases” at 00:43). Single grains and short layers of WP link up through the processes described in Finch et al. (2020) to create longer WP layers with increasing finite strain (supplementary movie: “Model\_sinistral\_phases” at 00:43). These long layers localise more strain than shorter layers, which has the effect of increasing overall strain localisation with increasing finite strain, as reflected in progressively higher  $F$  values (Fig. 6). Strain localisation initially increases rapidly with finite strain until  $\gamma = 4$ , when  $F = 0.6$ . After this point, the rate of increase reduces, and  $F$  begins to stabilise (Fig. 6). By  $\gamma = 10$ ,  $F = 0.66$ . We ran the model for another increment of shear strain to  $\gamma = 16$  to see whether localisation increased further and found that it remained steady, slightly below  $F \sim 0.7$ .

### 3.2. Models with initial dextral shearing $\gamma_{\text{dextral}} = 2$

The microstructural development of this model under D1 dextral shear was described in detail in Finch et al. (2020) as their ‘15WP\_Low’ model. Here we focus on the development of hybrid structures during D2.

At the end of dextral shearing in model  $\gamma_{\text{dextral}} = 2$ , grains of all phases are elongated and most form lozenge-shaped grains parallel to S planes, dipping left  $10$ – $40^\circ$  from the shear zone boundary (Fig. 2, Fig. 5g). The WP forms lozenges and fish parallel to the S plane with some tips parallel to the C plane (arrows in Fig. 2a). Unlike the other hybrid models described in the following sections, in this model there are no multi-grain layers of weak phase parallel to the shear zone boundary (C planes; Fig. 5g). There are a few grains of WP that form C planes, but these are isolated. The SP is more equant in shape than the other two phases, but most grains are elongate parallel to S planes ( $>90\%$ ; Fig. 2, Fig. 5g).

At the onset of sinistral shearing the left-dipping  $S_{\text{dextral}}$ -fabric begins to rotate anticlockwise to steeper angles (Fig. 2b). Strain localisation decreases because the left-dipping fabric is unfavourably oriented for sinistral shearing (Fig. 6). As sinistral shearing continues the shear sense inverts on weak phase grains and layers that formed  $S_{\text{dextral}}$  planes, so that they now form antithetic  $C''_{\text{sinistral}}$  shear bands that show left side up shear (supplementary movie: vertical high strain rate regions at 00:20 “Model\_dextral2\_strain”). These  $C''_{\text{sinistral}}$  shear bands localise some of the strain, and this causes the degree of strain localisation to stabilise, that is, strain localisation stops decreasing (Fig. 6 at  $\gamma_{\text{sinistral}} = 2$ ). By  $\gamma_{\text{sinistral}} = 2$  the grains have shortened and formed

equant shapes, which randomises the Feret angle since they no longer have a long axis (Fig. 5h).

Once layers of WP rotate into the stretching field, the grains become elongate, dipping to the right, and continue to rotate anticlockwise to become  $S_{\text{sinistral}}$  planes, dipping right  $10\text{--}40^\circ$  from the shear zone boundary (Fig. 2c arrows, 5i).  $S_{\text{sinistral}}$  planes rotate towards parallelism with the shear zone boundary. Where multiple WP grains are connected, they generally have a higher strain rate and rotate faster than isolated WP grains, so these are the first grains to become C planes (Fig. 2c; supplementary movie: “Model\_dextral2\_phases” at 00:30). Strain rate is highest in layers of weak phase that form C planes, and moderate in  $S_{\text{sinistral}}$  planes and short layers of weak phase that form C’ antithetic shear bands that accommodate rotation of lithons of stronger phases (supplementary movie: “Model\_dextral2\_strain” at 00:30).

Once C planes form, strain localisation increases dramatically, and continues to increase as more layers of WP rotate to become C planes and WP layers get longer (Fig. 6). This results in a reduction in strain rate on antithetic C’ shear bands and S planes, since C planes can accommodate higher strain rates than other structures (supplementary movie: “Model\_dextral2\_strain” at 00:44). As more layers of weak phase rotate to become C planes the strain localisation continues to increase, but the rate of increase reduces once  $F > 0.5$  (Fig. 6). By the end of the model, strain localisation has reached a steady state of around  $F = 0.62$ , which is lower than the final state of strain localisation reached in the other models. Once this steady state is reached the strain localisation factor  $F$  remains stable between  $F = 0.55$  and  $0.65$  (Fig. 6). By  $\gamma_{\text{sinistral}} = 8$ , the microstructure is similar to the sinistral shear only model at the same (sinistral) finite strain, with a well-developed S–C fabric and the majority of grains oriented  $<20^\circ$  from the shear zone boundary (S planes; Fig. 2e and 5l).

### 3.3. Models with initial dextral shearing of $\gamma_{\text{dextral}} = 4\text{--}14$

While there are differences between these models, commonalities in their evolution are discussed first.

#### 3.3.1. D1 microstructure

These models have a starting microstructure comprised of dextral S–C fabric, defined by layers of WP and IP with Feret angle maxima at  $10\text{--}30^\circ$  ( $S_{\text{dextral}}$  planes) and  $180^\circ$  (C planes; Fig. 3a, 5m and 5s). Grains of SP are lozenge-shaped and most are parallel to  $S_{\text{dextral}}$  planes (Fig. 3a, 5m and 5s). There are also C’ shear bands, defined mostly by layers of WP that rotated forwards in the direction of shear (WP planes at  $170^\circ$  in Figs. 5m, s; see Finch et al., 2020 15WP\_Low model for the full explanation of these structures during D1). Layers of WP parallel to the shear zone boundary increase in length with increasing D1 finite strain, so models that start with higher dextral finite strain have longer WP layers. Between the WP layers are layers or aggregates (lithons) of  $SP \pm IP$  (Fig. 3a). These layers of  $SP \pm IP$  can be parallel to C planes or can form poorly-defined  $\sigma$ -type objects with grains parallel to S planes (Fig. 3a; supplementary movie: “Model\_dextral6\_phases” at 00:40).

#### 3.3.2. D2 microstructure

Layers of WP undergo a different evolution to lithons of  $SP \pm IP$ , so the two are described separately. At the onset of sinistral shearing, C planes,  $S_{dextral}$  planes and  $C'_{dextral}$  shear bands in layers of WP respond differently. Some layers of WP that formed C planes invert their movement sense to sinistral shear, without a reduction in strain rate (Fig. 3b strain rate; supplementary movie: “Model\_dextral6\_strain” at 00:42). Other WP C planes are impeded by SP in the direction of shearing. These layers of WP shorten and fold (Fig. 3c, red arrows), and then lengthen to form S–C fabric that anastomoses around the impeding SP grains (Fig. 3d–f; supplementary movie: “Model\_dextral6\_phases” from 00:50).  $C'_{dextral}$  shear bands in WP undergo the same evolution as C planes because at the onset of sinistral shearing they rapidly rotate anticlockwise to form C planes (supplementary movie: “Model\_dextral6\_phases” from 00:40). Although  $S_{dextral}$  WP planes have the same orientation as  $C'_{sinistral}$  shear bands, very few  $S_{dextral}$  WP planes show an inversion of shear sense at the onset of sinistral shearing – that is, they do not become  $C'_{sinistral}$  shear bands. Instead, some  $S_{dextral}$  WP planes rotate backwards (clockwise) to become C planes. Later in the models, once folds are established in SP and IP aggregates, grains of WP tend to form cusped shapes that occupy areas between adjacent folds (Fig. 3c, red arrows).

Lithons of  $SP \pm IP$  that are parallel to C planes or  $S_{dextral}$  planes have a more complex evolution under sinistral shearing than layers of WP. Five main processes are observed comprising: (1) folding of lithons rotated into the maximum shortening direction (Fig. 3b–d), (2) folding of lithons by shearing on a WP C plane (Fig. 4, label [2]), (3) folding of SP layers between two WP layers (Fig. 4, label [3]), (4) rotation and folding of sigmoidal grains (Fig. 4, label [4]) and (5) internal shortening and rotation of lithons. These processes are described in turn.

- (1) During sinistral shearing, lithons comprised of multiple grains of  $SP \pm IP$  that are parallel to  $S_{dextral}$  planes rotate anticlockwise, in the direction of shear (Figs. 3b and 7) to steeper angles until they are parallel with the maximum shortening direction for sinistral shear. This causes folding, with axial planes perpendicular to the maximum shortening direction for sinistral shearing and approximately symmetrical fold geometries (Fig. 3c).
- (2) Lithons comprised of multiple grains of  $SP \pm IP$  that are parallel to  $S_{dextral}$  planes and have a high strain rate layer of WP directly above them can be sheared at the top of the lithon, causing an increase in stress in the top of the SP + IP layer and dragging of the top of the left-dipping lithon to the left (Fig. 4, label [2], upper SP layer). This can also occur at the base of the lithon adjacent to a rotating lithon (Fig. 4, label [2], lower SP layer), although this is rarer. This produces asymmetric, isoclinal or hook folds (Fig. 4c).
- (3) Layers of SP that are between two layers of WP can undergo a third type of folding, where they are shortened between two high strain rate WP layers (Fig. 4, label [3], red arrows denote high strain rate layers). This produces disharmonic folds with an overall S-shaped asymmetry with vergence to the left.
- (4) Lithons of SP that are comprised of a few grains that form  $\sigma_{dextral}$  objects, or single grains of SP that form  $\sigma_{dextral}$  clasts within an IP matrix, can rotate anticlockwise so that their long axis is vertical and tips are tightly folded (Fig. 4, label [4] and Fig. 8e and f). These grains then shorten and form S-folds with axial planes at a

small angle with the C plane. Folds continue to rotate until the long limb of the S fold rotates into parallelism with the shear zone boundary, which then causes an increase in strain rate in the C-parallel limb, shearing apart the hinges of the fold.

- (5) Lithons of SP that are parallel to  $S_{\text{dextral}}$  planes or single grains of SP can also shorten to form more equant shapes and then form  $\sigma_{\text{sinistral}}$  objects (e.g., Fig. 3e and f red arrows).

Process 1 is dominant in the  $\gamma_{\text{dextral}} = 4$  model, but is less important in the  $\gamma_{\text{dextral}} = 6$  and 8 models and is rare in the  $\gamma_{\text{dextral}} = 10\text{--}14$  models. Within each model, small sections undergo these processes at different times, and rotation and transposition occur at different rates, dependent on proximity to a high strain rate layer of WP as well as processes occurring in neighbouring sections of the model. This produces conflicting shear sense indicators (i.e., sinistral and dextral shear sense indicators at the same finite strain, see supplementary movie: “Model\_dextral6\_phases” at time 01:28), disharmonic folds (when one part of layer folds before or differently to the rest of the layer) and different parts of the model deformed in different ways at the same finite strain (e.g., Fig. 4). Lithons of  $SP \pm IP$  parallel to  $S_{\text{dextral}}$  planes that are sandwiched between long WP C planes rotate fastest and are folded first (e.g., Fig. 4b, red arrows). This indicates that rotation is a mechanical response to high strain rate on C planes. Within these  $SP \pm IP$  domains there are sparse grains of WP, which are in-folded and then cause slip and shearing on fold limbs. These grains and short layers typically have cusped shapes, infilling the space between folded layers (Fig. 3c red arrows).

While most asymmetric folds in these models have an S-shaped geometry, rare Z-folds also form due to drag folding on the limb of a pre-existing fold. Thus, the asymmetry of folds cannot reliably be used as a shear sense indicator, as previously highlighted by Llorens et al. (2013). After folds form, through processes 1–4, they rotate anticlockwise, forming S-folds and disharmonic folds with a variety of shapes and opening angles, from isoclinal to open, but becoming tighter as shearing progresses (Fig. 3d). As folds rotate and tighten, their amplitude increases and axial planes approach parallelism with the shear zone boundary. Eventually, once transposition is complete, all remaining folds are isoclinal and most hinges have been sheared apart from limbs, forming hooks and rootless isoclinal folds, with dismembered limbs forming S–C fabric (Fig. 3e and f).

### 3.3.3. Differences between the hybrid models

At the beginning of dextral shearing the microstructure is a heterogeneous mix of phases (Fig. 1) and through dextral shearing the phases link up and form compositional layering (E.g., supplementary material “model\_dextral14\_phases” from start to 1:00). This happens because grains of WP that rotated into parallelism with the shear zone boundary are at high strain rate, which causes high stress at their tips, in grains of IP and SP (Finch et al., 2020). Deformation focuses into these high stress regions, allowing grains of WP to link up into layers that increase in length with strain. Thus, with more D1 strain, layers of WP become longer and more numerous, which localises more strain to them. The number and length of WP layers is the major cause of differences in the microstructure between the low and high dextral finite strain models at the end of dextral shearing. The  $\gamma_{\text{dextral}} = 2$  model has low interconnectivity of WP grains at the end of dextral shearing (Fig. 2a) and lower strain localisation (Fig. 6) whereas the  $\gamma_{\text{dextral}} = 14$  model has high interconnectivity of WP grains and higher strain localisation than the other models (Fig.

6).

In the  $\gamma_{\text{dextral}} = 2$  model finite strain during dextral shearing was too low to rotate WP grains into parallelism with the shear zone boundary, so there is no compositional layering and no WP C planes. The microstructure consists of a heterogenous mix of phases that form  $S_{\text{dextral}}$  planes, which rotate anticlockwise into the maximum shortening direction during sinistral shear. The individual grains shorten to equant shapes, and then elongate in the direction of maximum stretching to form  $S_{\text{sinistral}}$  planes (Fig. 2a–c).

In contrast to the  $\gamma_{\text{dextral}} = 2$  model, models with higher dextral finite strain feature C planes of WP and more pronounced compositional layering. While these models show rapid rotation of  $S_{\text{dextral}}$  planes from  $\gamma_{\text{sinistral}} = 0.02$  to  $\gamma_{\text{sinistral}} = 2$  (Fig. 7b–d), unlike the  $\gamma_{\text{dextral}} = 2$  model, not all areas of the model rotate at the same rate. Once  $S_{\text{dextral}}$  planes rotate into the maximum shortening field they fold, as described previously.

Another difference between models is the timing of when folds first form. In the  $\gamma_{\text{dextral}} = 4$  model, folds form before  $\gamma_{\text{sinistral}} = 2$  (Fig. 7b), whereas in the  $\gamma_{\text{dextral}} = 6$  model they do not form until  $\gamma_{\text{sinistral}} = 2.8$ . In the  $\gamma_{\text{dextral}} = 8$  model they form from  $\gamma_{\text{sinistral}} = 3$ , whereas in the  $\gamma_{\text{dextral}} = 10$  and 12 models they form at  $\gamma_{\text{sinistral}} = 3.6$ – $3.8$ . Thus, folds form at higher D2 strain in the models that experienced higher D1 finite strain.

Models with lower  $\gamma_{\text{dextral}}$  also show a lower proportion of  $S_{\text{sinistral}}$  planes at  $\gamma_{\text{sinistral}} = 2$  (i.e., Feret angle  $\sim 135^\circ$ – $170^\circ$ ; Fig. 7h percentages inside graphs) than models with higher  $\gamma_{\text{dextral}}$ . This implies that models with high dextral finite strain show quicker transposition to a sinistral microstructure.

The models also show markedly different evolutions in strain localisation during D2 sinistral shearing (Fig. 6). Models with low finite strain ( $\gamma_{\text{dextral}} = 2$  and 4) showed a pronounced reduction in strain localisation at the commencement of sinistral shearing ( $\Delta F \sim 0.2$ ; Fig. 6). For the  $\gamma_{\text{dextral}} = 2$  model localisation decreased from 0.45 at the end of dextral shearing to 0.25 at  $\gamma_{\text{sinistral}} = 2$ . The  $\gamma_{\text{dextral}} = 4$  showed a similar reduction but over a longer time period, from  $F = 0.68$  at the end of dextral shearing to 0.48 at  $\gamma_{\text{sinistral}} = 4$ . The other models also showed a more modest reduction in strain localisation at the onset of sinistral shearing with a  $\Delta F$  between 0.05 and 0.1.

## 4. Discussion

Shear zones that are reactivated with opposite, co-planar shear sense show complex and dynamic interference patterns, with parts of a single model undergoing different types of deformation at different times due to heterogenous distribution of strain rate and stress. While the general evolution of most models was similar, there were differences in the timing of the major stages of microstructural evolution between the models, and these differences reveal how the pre-existing microstructure produced during dextral shearing influences the interference patterns and structural evolution. We explore these differences between the models before comparing our models to a naturally deformed shear zone.

### 4.1. Differences in the evolution of models

As highlighted in section 3.4, the effect of more finite strain during D1 ( $\gamma_{\text{dextral}}$ ) is the creation of longer layers of WP parallel to the shear zone boundary, and better developed

compositional layering. The  $\gamma_{\text{dextral}} = 2$  model, with the lowest D1 finite strain, shows an unusual microstructure in the early stages of D2, where the rotation of former  $S_{\text{dextral}}$  planes into the maximum shortening field causes grains to shorten and form equant shapes. The cause of this difference is the absence of layering and the homogenous dispersal of phases in the  $\gamma_{\text{dextral}} = 2$  model, which means that the model deforms homogeneously (Fig. 2a–c). As far as we know, the microstructure seen in the  $\gamma_{\text{dextral}} = 2$  model has never been observed in nature, but the transition occurs so rapidly that it may be rarely preserved or recognised. The  $\gamma_{\text{dextral}} = 4$  and 6 models undergo the same rotation of  $S_{\text{dextral}}$  planes into the maximum shortening field as the  $\gamma_{\text{dextral}} = 2$  model, but in these models shortening causes folding rather than the development of equant grains. This is because  $S_{\text{dextral}}$  planes are dominantly competent layers of  $SP \pm IP$ , which respond to shortening as layers that fold.

While the  $\gamma_{\text{dextral}} = 8–14$  models show asymmetric intrafolial folds during dextral shearing, folding of  $S_{\text{dextral}}$  planes during sinistral shearing is rare or absent in these models, which have a higher proportion of WP parallel to the shear zone boundary. These models also contain more  $C'_{\text{dextral}}$  shear bands, since these form through the rotation of C planes forwards in the direction of shearing (Finch et al., 2020). C planes and  $C'_{\text{dextral}}$  shear bands can simply invert shear sense to accommodate sinistral shearing (as C planes and  $S_{\text{sinistral}}$  planes, respectively), which means these models can accommodate sinistral shearing during D2 more efficiently and with a lower drop in strain localisation than in the  $\gamma_{\text{dextral}} = 2$  and 4 models (Fig. 6). However, some of these WP C planes are impeded on their left side by grains of SP, so there is a small reduction in strain rate until the WP layers can overcome this impediment (e.g., strain rate increase in layer of WP in Fig. 4b (bottom red arrow) compared to Fig. 4a as the layer finds a path through the SP by Fig. 4c). The higher abundance of  $C'_{\text{dextral}}$  shear bands in the  $\gamma_{\text{dextral}} = 8–14$  models also explains why these models have a higher proportion of  $S_{\text{sinistral}}$  planes by  $\gamma_{\text{sinistral}} = 2$ , since these dextral shear bands can simply invert shear direction to become  $S_{\text{sinistral}}$  planes (Fig. 7h).

Extrapolating to a natural setting, this suggests that the highest strain shear zones with well-developed C planes may preferentially localise shearing under an inversion of shear sense. While ductile shear zones have long been recognised as weak zones prone to reactivation, this work demonstrates the specific structures that most efficiently accommodate shear reversal, and therefore the shear zones that are most likely to reactivate, when all other factors are equal (e.g., same rheology, T, P, orientation etc).

## 4.2. A dynamic atlas of shear zone interference microstructures

During the transposition of a dextral microstructure to a sinistral microstructure there is a period of transition where shear zone interference patterns are observed. The shear zone interference patterns generated are dynamic and evolve dramatically during sinistral shearing. To understand the full evolution, visualisation of the incremental strain is needed, which is why a ‘dynamic atlas’ is required to understand shear zone interference microstructures. In the supplementary material we provide movies of the microstructure, strain rate and stress of each hybrid model, which form this dynamic atlas. We envisage that in future, researchers who suspect they may be dealing with shear zone interference patterns will be able to compare their structures to our models and to understand how the natural examples evolved.

Although the atlas is dynamic, we are able to identify a few key moments in the microstructural evolution that capture the essence of the main processes, as highlighted in Fig. 2, Fig. 3, Fig. 4. During the period of transition from D1 structures to D2 structures, the models show a high degree of microstructural variability, as depicted in Fig. 4 with three SP layers in close proximity being folded at the same time but through different mechanisms. To understand this variable deformation of the SP, it is necessary to consider the distribution of strain rate and stress. Layers of SP are low strain rate, but commonly adjacent to layers of WP that accommodate high strain rates (Fig. 4). Strain localisation in these models is dynamic, with the locus of maximum strain rate frequently jumping between different layers of WP. In our models, layers of SP  $\pm$  IP deform and rotate when nearby layers of WP accommodate high strain rate, causing an increase in stress in the SP + IP layers, which drives deformation (Fig. 4). Heterogeneities in the shape of the SP + IP lithon and stress create torque that cause it to rotate.

In section 3.3.2 we identified five ways that the SP  $\pm$  IP layers in the models deform. SP layers that have WP layers adjacent tend to form hook folds (Fig. 4, process 2), whereas if a layer of SP is sandwiched between two WP layers it is more likely to form asymmetric, disharmonic folds (Fig. 4, process 3). Small layers or isolated grains of SP that occur in a matrix of IP tend to be more likely to form rotated  $\sigma$ -objects (Fig. 4, process 4). When there are only a small number of WP C planes, or when there is a more homogenous distribution of phases, SP + IP layers have WP in them and tend to form more symmetrical folds, through the rotation of  $S_{\text{dextral}}$  planes into the maximum shortening direction (Fig. 3).

### 4.3. Comparison with naturally deformed shear zones

The models in this paper are mechanical and do not incorporate recrystallisation, grain boundary sliding and a number of other strain softening and hardening processes that occur in naturally deformed shear zones. To ensure they capture the most essential features of the natural processes it is useful to compare our results to natural case studies of reactivated shear zones from Zanskar, NW India (Finch et al., 2014) and Askvik, Norway (Wennberg, 1996). The Zanskar shear zone is a ductile, normal-sense shear zone, an extension of the South Tibetan Detachment System with similar timing and nature. Prior to normal shearing, the shear zone had a thrust shear sense, which is preserved in the footwall and hanging wall and overprints normal shearing. Finch et al. (2014) determined that thrusting and normal shearing were coplanar and codirectional with a simple inversion in shear sense. This zone of overprinting is preserved in their structural domain 3, which consists dominantly of biotite-muscovite pelitic schists of the Tethyan sedimentary series. In outcrop, thrust-sense S–C fabric is overprinted by sharp, normal sense shear planes or brittle faults (Fig. 10 in Finch et al., 2014).

In a thin section from the Zanskar shear zone, a range of hybrid microstructures and shear zone interference structures are evident (Fig. 8). Sheared fold trains form in layers of mixed biotite and quartz (Fig. 8a). These are also seen in the hybrid models (Fig. 8b), where they form when  $S_{\text{dextral}}$  planes are rotated to steep angles during sinistral shearing, folded and then folds rotated due to shearing on adjacent layers of WP (Fig. 8c). The Zanskar shear zone thin section also shows rotated  $\sigma_{\text{dextral}}$  clasts (Fig. 8d), similar to the lozenge-shaped quartz veins in Wennberg (1996) that are rotated and tips folded during D2. These are also seen in our models (Fig. 8e and f) where they form due to anticlockwise rotation of  $\sigma_{\text{dextral}}$  clasts. Disharmonic folds are evident in the Zanskar shear

zone thin section in layers of quartz, which is the strongest phase in the rock (Fig. 8g). Layers of biotite are infolded and form cusped shapes, flowing around the folded quartz layers. These features are also seen in the transition zone of the Bergen Arc shear zone (Wennberg, 1996) as well as our models (Fig. 8h). The Zanskar shear zone thin section also shows a variety of different fold types from open to isoclinal with a range of axial plane orientations (Fig. 8i), which are also evident in our models (Fig. 3, Fig. 4). Thus, it appears that the models replicate the structures that form in naturally deformed shear zones.

Wennberg's (1996) account of the Bergen Arc shear zone affords the unique opportunity to observe how D1 structures were modified by a coplanar, opposite sense D2, since both shear zones are preserved and there is a zone of interference at their boundary. The sinistral shear zone (D1) shows S–C' fabric and quartz veins with pinch-and-swell structures or lozenge-shapes parallel to S planes with tails deflected into C' shear bands. In the transition zone, dextral shearing (D2) caused S-planes and C' shear bands to invert shear sense, so that S planes that underwent top-up sinistral shearing during D1, showed top-down dextral shearing during D2 and C' shear bands that showed top-down sinistral shearing during D1 inverted to top-up dextral shearing during D2. S planes and C' shear bands that developed during D1 rotated clockwise during D2 dextral shearing, but S surfaces rotated faster than C' shear bands, so the angle between them decreased with increasing finite strain (i.e., towards the centre of the dextral Bergen Arc shear zone). In thin section, S surfaces showed asymmetric folds locally with dextral vergence (Z-folds), which we also observed in our hybrid models (Fig. 8c). Lozenge-shaped quartz veins rotated clockwise to steeper angles and their tips became tightly folded. Longer quartz veins that formed pinch-and-swell structures in sinistral shearing were rotated clockwise and, on the microscale, folded asymmetrically. Folds are disharmonic, open to tight and have a thin and a thick limb, corresponding to former 'pinch' zones and 'swell' zones, respectively. These folded lozenges are analogous to our SP grains that formed rotated  $\sigma$ -clasts (Fig. 8e and f). Moving out of the transition zone and into the higher strain section of the dextral shear zone, microstructures are of the same type as those in the zone of sinistral shearing outside the Bergen Arc shear zone, but with opposite orientation and sense of shear.

There are also some differences between our models and the naturally deformed examples from the Zanskar and Bergen Arc shear zones. Both natural shear zones feature discontinuous layers of quartz that behave as competent layers. We were able to replicate the major structures seen in these quartz layers in our single grains of SP and/or lithons of IP + SP. However, in the natural samples these quartz layers tend to control the deformation more than the SP does in our models, so we do not see exact replication of the natural structures observed. Wennberg (1996) also found that D1 S planes and C' shear bands underwent a simple inversion of shear sense in D2. While in our models some C'<sub>dextral</sub> shear bands inverted shear direction to form S<sub>sinistral</sub> planes, they more commonly rotated to form C planes at the onset of D2. The S<sub>dextral</sub> planes also rotated to form C planes at the onset of D2, or they rotated into the shortening field and folded. One possible explanation for this is the difference between our models and the shear zone in Wennberg (1996) at the end of D1 shearing. The latter was dominated by S–C' fabric whereas our models showed S–C fabric. In our models we see that high strain rate on C planes causes high stress in SP + IP lithons, which causes them to rotate. The absence of C planes in the shear zone of Wennberg (1996) may have produced more homogenous deformation and less rotation. In our models we have also not explored the effects of parameters that

would likely affect the interference structures, such as different proportions of the three phases and the presence of pre-existing layering, which will be avenues for future research.

## 5. Conclusion

Using numerical modelling, we determined the interference patterns that develop when ductile simple shearing is overprinted by co-planar shearing with opposite sense. Models with low D1 finite strain deformed more homogeneously by either shortening individual grains, or forming symmetric folds. For models with D1  $\gamma$  values of 6–14 the microstructural evolution during D2 was controlled by the distribution of WP layers. Grains and lithons of SP  $\pm$  IP are folded, rotated or stretched depending on their proximity to WP layers and the strain rate of the WP layer relative to other layers. Models with higher D1 strain showed a higher proportion of sinistral structures by  $\gamma_{\text{sinistral}} = 2$  and a smaller decrease in strain localisation, which suggests that high D1 strain models could more easily accommodate D2 strain. This is largely due to a higher abundance of WP C planes in the higher strain models, which have the same orientation in co-planar shear zones of opposite sense. We identified a range of shear zone interference structures that form due to the superposition of D2 on D1 and these are documented completely in the dynamic atlas: a series of movies in the supplementary material that can be used to compare to naturally deformed rocks to understand how hybrid structures form.

### Credit statement

M. A. Finch: Conceptualisation, methodology, software, formal analysis, investigation, resources, data curation, writing – original draft, writing – review & editing, visualisation.

P.D. Bons: Software, resources, writing – review & editing.

R.F. Weinberg: resources, writing – review & editing, project administration.

M.G. Llorens: Software, writing – review & editing.

A. Griera: Software, writing – review & editing.

E. Gomez-Rivas: Software, writing – review & editing.

### Declaration of competing interest

The authors declare that they have no known competing financial interests or personal relationships that could have appeared to influence the work reported in this paper.

### Acknowledgements

We wish to acknowledge Ricardo A. Lebensohn for development of VPFIT and part of the ELLE platform and Florian Steinbach for the generation of code for ELLE that is used in this paper. We would also like to acknowledge an excellent, constructive review from Robyn Gardener and an anonymous reviewer.

## Data availability

Data will be made available on request.

## References

- Berthe, D., Choukroune, P., Jegouzo, P., 1979. Orthogneiss, mylonite and non coaxial deformation of granites: the example of the South Armorican Shear Zone. *J. Struct. Geol.* 1, 31–42.
- Bons, P.D., Koehn, D., Jessell, M.W., 2008. Microdynamics simulation. In: Bhattacharji, S., Neugebauer, H.J., Reitner, J., Stüwe, K. (Eds.), *Lecture Notes in Earth Sciences*. Springer-Verlag, Berlin, p. 405.
- Collins, W.J., 2002. Hot orogens, tectonic switching, and creation of continental crust. *Geology* 30, 535–538.
- Cooper, F.J., Platt, J.P., Platzman, E.S., Grove, M.J., Seward, G., 2010. Opposing shear senses in a subdetachment mylonite zone: implications for core complex mechanics. *Tectonics* 29.
- Dutta, D., Mukherjee, S., 2019. Opposite shear senses: geneses, global occurrences, numerical simulations and a case study from the Indian western Himalaya. *J. Struct. Geol.* 126, 357–392.
- Finch, M., Hasalov' a, P., Weinberg, R.F., Fanning, C.M., 2014. Switch from thrusting to normal shearing in the Zaskar shear zone, NW Himalaya: implications for channel flow. *Geol. Soc. Am. Bull.* 126, 892–924.
- Finch, M.A., Bons, P.D., Steinbach, F., Griera, A., Llorens, M.G., Gomez-Rivas, E., Ran, H., de Riese, T., 2020. The ephemeral development of C' shear bands: a numerical modelling approach. *J. Struct. Geol.* 139, 104091.
- Gomez-Rivas, E., Griera, A., Llorens, M.-G., Bons, P.D., Lebensohn, R.A., Piazzolo, S., 2017. Subgrain rotation recrystallization during shearing: insights from full-field numerical simulations of halite polycrystals. *J. Geophys. Res. Solid Earth* 122, 8810–8827.
- Grasemann, B., Stüwe, K., 2001. The development of flanking folds during simple shear and their use as kinematic indicators. *J. Struct. Geol.* 23, 715–724.
- Griera, A., Bons, P.D., Jessell, M.W., Lebensohn, R.A., Evans, L., Gomez-Rivas, E., 2011. Strain localization and porphyroclast rotation. *Geology* 39, 275–278.
- Griera, A., Gomez-Rivas, E., Llorens, M.-G., 2020. The influence of layer-interface geometry on single-layer folding. *Geol. Soc. Lond. Spec. Publ.* 487, 59.
- Griera, A., Llorens, M.-G., Gomez-Rivas, E., Bons, P.D., Jessell, M.W., Evans, L.A., Lebensohn, R., 2013. Numerical modelling of porphyroclast and porphyroblast rotation in anisotropic rocks. *Tectonophysics* 587, 4–29.
- Holyoke, C.W., Tullis, J., 2006. Mechanisms of weak phase interconnection and the effects of phase strength contrast on fabric development. *J. Struct. Geol.* 28, 621–640.
- Hyndman, R.D., Currie, C.A., Mazzotti, S.P., 2005. Subduction zone backarcs, mobile belts and orogenic heat. *GSA Today (Geol. Soc. Am.)* 15, 4–10.
- Jessell, M.W., Bons, P.D., Evans, L., Barr, T., Stüwe, K., 2001. Elle: a micro-process

- approach to the simulation of microstructures. *Comput. Geosci.* 27, 17–30.
- Lebensohn, R.A., 2001. N-site modeling of a 3D viscoplastic polycrystal using fast Fourier transform. *Acta Mater.* 49, 2723–2737.
- Lebensohn, R.A., Brenner, R., Castelnau, O., Rollett, A.D., 2008. Orientation image-based micromechanical modelling of subgrain texture evolution in polycrystalline copper. *Acta Mater.* 56, 3914–3926.
- Lebensohn, R.A., Montagnat, M., Mansuy, P., Duval, P., Meysonnier, J., Philip, A., 2009. Modeling viscoplastic behavior and heterogeneous intracrystalline deformation of columnar ice polycrystals. *Acta Mater.* 57, 1405–1415.
- Lebensohn, R.A., Rollett, A.D., 2020. Spectral methods for full-field micromechanical modelling of polycrystalline materials. *Comput. Mater. Sci.* 173, 109336.
- Lister, G.S., Snoke, A.W., 1984. S-C mylonites. *J. Struct. Geol.* 6, 617–638.
- Llorens, M.-G., Bons, P.D., Griera, A., Gomez-Rivas, E., Evans, L.A., 2013. Single layer folding in simple shear. *J. Struct. Geol.* 50, 209–220.
- Llorens, M.-G., Gomez-Rivas, E., Ganzhorn, A.-C., Griera, A., Steinbach, F., Roessiger, J., Labrousse, L., Walte, N.P., Weikusat, I., Bons, P.D., 2019. The effect of dynamic recrystallisation on the rheology and microstructures of partially molten rocks. *J. Struct. Geol.* 118, 224–235.
- Llorens, M.-G., Griera, A., Bons, P.D., Lebensohn, R.A., Evans, L.A., Jansen, D., Weikusat, I., 2016a. Full-field predictions of ice dynamic recrystallisation under simple shear conditions. *Earth Planet Sci. Lett.* 450, 233–242.
- Llorens, M.-G., Griera, A., Bons, P.D., Roessiger, J., Lebensohn, R.A., Evans, L., Weikusat, I., 2016b. Dynamic recrystallisation of ice aggregates during co-axial viscoplastic deformation: a numerical approach. *J. Glaciol.* 62, 359–377.
- Llorens, M.-G., Griera, A., Steinbach, F., Bons, P.D., Gomez-Rivas, E., Jansen, D., Roessiger, J., Lebensohn, R.A., Weikusat, I., 2017. Dynamic recrystallization during deformation of polycrystalline ice: insights from numerical simulations. *Phil. Trans. Math. Phys. Eng. Sci.* 375, 20150346.
- Montagnat, M., Castelnau, O., Bons, P.D., Faria, S.H., Gagliardini, O., Gillet-Chaulet, F., Grennerat, F., Griera, A., Lebensohn, R.A., Moulinec, H., Roessiger, J., Suquet, P., 2014. Multiscale modeling of ice deformation behavior. *J. Struct. Geol.* 61, 78–108.
- Murphy, F.C., Hutton, L.J., Walshe, J.L., Cleverley, J.S., Kendrick, M.A., McLellan, J., Rubenach, M.J., Oliver, N.H.S., Gessner, K., Bierlein, F.P., Jupp, B., Aill'eres, L., Laukamp, C., Roy, I.G., Miller, J.M., Keys, D., Nortje, G.S., 2011. Mineral system analysis of the Mt isa–McArthur river region, northern Australia. *Aust. J. Earth Sci.* 58, 849–873.
- Passchier, C.W., Simpson, C., 1986. Porphyroclast systems as kinematic indicators. *J. Struct. Geol.* 8, 831–843.
- Piazolo, S., Bons, P.D., Griera, A., Llorens, M.G., Gomez-Rivas, E., Koehn, D., Wheeler, J., Gardner, R., Godinho, J.R.A., Evans, L., Lebensohn, R.A., Jessell, M.W., 2019, 111-123. A review of numerical modelling of the dynamics of microstructural development in rocks and ice: past, present and future. *J. Struct. Geol.* 125.
- Ramsay, J.G., 1962. Interference patterns produced by the superposition of folds of

- similar types. *J. Geol.* 70, 466–481.
- Ran, H., Bons, P.D., Wang, G., Steinbach, F., Finch, M.A., Griera, A., Gomez-Rivas, E., Llorens, M.-G., Ran, S., Liang, X., Zhou, J., 2018. High-strain deformation of conglomerates: Numerical modelling, strain analysis, and an example from the Wutai Mountains. *North China Craton. J. Struct. Geol.* 114, 222–234.
- Roberts, A.G., Weinberg, R.F., Hunter, N.J.R., 2022. Normal reactivation of the main central thrust zone in Sikkim Himalaya. *J. Asian Earth Sci.* 228, 105139.
- Schneider, C.A., Rasband, W.S., Eliceiri, K.W., 2012. NIH Image to ImageJ: 25 years of image analysis. *Nat. Methods* 9, 671–675.
- Steinbach, F., Bons, P.D., Griera, A., Jansen, D., Llorens, M.-G., Roessiger, J., Weikusat, I., 2016. Strain localisation and dynamic recrystallisation in the ice-air aggregate: a numerical study. *Cryosphere* 10, 3071–3089.
- Trevisan, V.G., Hagemann, S.G., Loucks, R.R., Xavier, R.P., Motta, J.G., Parra-Avila, L.A., Petersson, A., Gao, J.-F., Kemp, A.I.S., Assis, R.R., 2021. Tectonic switches recorded in a paleoproterozoic accretionary orogen in the alta floresta mineral province, southern amazonian craton. *Precambrian Res.* 364, 106324.
- Wennberg, O.P., 1996. Superimposed fabrics due to reversal of shear sense: an example from the Bergen Arc shear zone, western Norway. *J. Struct. Geol.* 18, 871–889.
- White, S.H., Bretan, P.G., Rutter, E.H., 1986. Fault-zone reactivation: kinematics and mechanisms. *Phil. Trans. Roy. Soc. Lond. Math. Phys. Sci.* 317, 81–97.
- Yan, D.-P., Kong, R., Dong, X., Qiu, L., Liu, H., 2021, 1537-1556. Late jurassic-early cretaceous tectonic switching in liaodong peninsula of the north China craton and the implications for gold mineralisation. *Sci. China Earth Sci.* 64.